Improving bifunctional activities of self-assembled nanostructured $CuCo_2O_4$ for electrochemical energy storage and the oxygen evolution reaction via morphology engineering

Abu Talha Aqueel Ahmed,[1] Bo Hou,[2] Harish. S. Chavan,[1] Yongcheol Jo,[1] Sangeun Cho,[1] Jongmin Kim,[1] Sambhaji M. Pawar,[1] SeungNam Cha,[2] Akbar I. Inamdar,[1] Hyungsang Kim,*[1] Hyunsik Im**

[1]Division of Physics and Semiconductor Science, Dongguk University, Seoul 04620, South Korea

[2]Department of Engineering Science, University of Oxford, Parks Road, OX1 3PJ, UK

E-mail: akbarphysics2002@gmail.com, hyunsik7@dongguk.edu, hskim@dongguk.edu

Keywords: $CuCo_2O_4$, hydrothermal growth, morphology tuning, electrochemical supercapacitor, oxygen evolution reaction

Abstract

$CuCo_2O_4$ films with different morphologies of either mesoporous nanosheet, cubic, compact-granular, or agglomerated embossing structures are fabricated via a hydrothermal growth technique using various solvents, namely deionized water, ethanol, ethylene glycol, and glycerol, and their bifunctional activities, electrochemical energy storage and oxygen evolution reactions (OERs) for water splitting catalysis in strong alkaline KOH media are investigated. We observed that the solvents played an important role in setting the surface morphology and size of the crystallites by controlling nucleation and growth rate. An optimized mesoporous $CuCo_2O_4$ nanosheet electrode shows a high specific capacitance of 1,658 F g^{-1} at a current density of 1 A g^{-1} with excellent restoring capability of ~ 99% at 2 A g^{-1} and superior energy density of 132.64 Wh kg^{-1} at a power density of 0.72 kW kg^{-1} .The $CuCo_2O_4$ electrode also

exhibits excellent endurance performance with capacity retention of 90% and coulombic efficiency of ~ 99% after 5,000 charge/discharge cycles. The best OER activity is obtained from $CuCo_2O_4$ nanosheet sample with the lowest overpotential of 294 mV at 20 mA cm^{-2} and a Tafel slope of 117 mV dec^{-1}. The superior bifunctional electrochemical activity of the mesoporous $CuCo_2O_4$ nanosheet is a result of electrochemically favorable 2D morphology, which lead to the formation of a very large electrochemically active surface area.

Introduction

Among various energy conversion and storage devices,[1,2] supercapacitors (SCs) with features such as fast charge/discharge rate, high power density, a wide operating temperature range, long lifespan, and good safety have become typically highlighted as one of the most convenient choices for energy storage devices in the past decades.[3-23] Moreover, these excellent properties have made it possible to utilize them in various applications such as computer-memory backup systems, portable electronics, industrial-scale power, communication networks, hybrid-electric vehicles, and energy management.[24-39] On the other hand, electrochemical water splitting (EWS) is considered as an efficient way to produce oxygen and hydrogen for clean fuel cells. This process can be categorized into two main half-cell reactions: the oxygen evolution reaction (OER) that occurs at the anode and the hydrogen evolution reaction (HER) at the cathode, both of which are crucial for overall full water splitting efficiency. Although, the H_2 production from electrocatalytic water splitting is relatively easy, O_2 production is more complicated and requires more overpotential than the theoretical potential value (1.23 V) due to sluggish kinetics. Therefore, an electrocatalyst is needed to increase the reaction rate and to reduce the overpotential. Recently, Ru and Ir-based precious metal oxides have exhibited good OER activity in alkaline as well as acidic media, but their high cost and low abundance have greatly hampered their practical application. Hence, the

development of earth-abundant, inexpensive, and efficient OER electrocatalysts with a low overpotential is required for the OER to replace noble metal based catalysts.

Transition metal oxides have attracted a lot of attention as multifunctional electrodes for SCs and EWS. Transition metal oxides have multiple oxidation states, which can result in good electrochemical activity and catalytic properties.[40] Although they suffer from intrinsically low electrical conductivity and the fact that their Faradaic reactions are fast at high current density rates and only occur at the electrode surface due to limited diffusion.[41,42] These disadvantages inhibit their application in practical high-rate SCs and efficient EWS. Latterly, binary copper cobalt oxide and its hybrid materials have been utilized as active electrodes with considerably improved supercapacitive electrochemical performance compared with single metal oxides. This is because both anions can contribute to the Faradaic redox mechanism for pseudocapacitance.[43-44] Moreover, novel strategies or materials are needed to enhance the electrochemical performance of electrode materials for high rate power applications and low overpotential, including utilization of the synergistic effects of hybrid materials or the fabrication of nanoengineered structures.[45] Especially, it is known that the morphology of electrode materials can greatly influence their performance because electrochemically active sites for the Faradaic redox reaction are proportional to the specific surface area.[20] Thus, a strategy for developing electrode materials maximizes their specific surface area via morphology engineering without sacrificing other material properties should be made.

In the present work, we report the binder-free, shape-controlled synthesis of $CuCo_2O_4$ on Ni foam via a facile hydrothermal method using different solvents. We demonstrate that an optimized nanosheet $CuCo_2O_4$ electrode attained a high specific capacitance of 1658 F g^{-1} at 1 A g^{-1} (974 F g^{-1} at 20 A g^{-1}), high energy density of 132.64 Wh kg^{-1} at a power density of ~ 0.72 kW kg^{-1}, and superior long-term capacity retention of ~ 90% after 5,000 charge-discharge cycles at a high current density of 20 A g^{-1}. Moreover, it exhibited good EWS properties with a low overpotential of 294 mV at 20 mA cm^{-2} and a Tafel slope of 117 mV dec^{-1} in 1 M KOH.

Results and Discussions

XRD measurements were performed to investigate the crystal phase formation of the $CuCo_2O_4$ as shown in Figure 1a. Multiple diffraction peaks in the XRD spectra indicated the polycrystalline nature of the films, and it can be clearly seen that the diffraction peaks of CCO_{nS}, CCO_C, CCO_G, and CCO_S film samples were perfectly indexed to the cubic phase of $CuCo_2O_4$ (JCPDS card no. 01-1155). The diffraction peaks at 19.16°, 31.34°, 36.98°, 38.58°, 44.82°, 55.7°, 59.36°, and 65.62° corresponded to reflections of the (111), (220), (311), (222), (400), (422), (511) and (440) planes of $CuCo_2O_4$, respectively. The almost similar XRD spectra suggest that the used solvents did not affect the crystal phase and crystallinity of $CuCo_2O_4$ but modified the surface morphology instead while the absence of other noticeable diffraction peaks confirms the phase purity of $CuCo_2O_4$. Furthermore, EDS and XPS spectroscopies was carried out to confirm the composition and to distinguish between our samples, and Figure 1b, the EDS spectra revealed that the core Cu, Co and O elements existed stoichiometrically in the films, which was confirmed by the XPS analysis (Figure S1). In addition, the binding states of Cu^{2+}, Co^{3+}, and O^{2-} confirmed the formation of $CuCo_2O_4$.

Figure 2 shows SEM images of the $CuCo_2O_4$ films synthesized using different solvents, whereby completely different morphologies were obtained with each one. The CCO_{nS} electrode film comprised mesoporous sheet-like morphology (Figure 2a) with a thickness below ~ 30 nm, while the CCO_C electrode was composed of cubic-like morphology with numerous ordered interconnected particles (Figure 2b). The morphology of the CCO film synthesized with ethylene glycol (CCO_G) consisted of a compact granular-like structure (Figure 2c). Furthermore, the CCO_S film fabricated with glycerol was constructed from numerous agglomerated spherical particles of different diameters interconnected with each other with (Figure 2d). It seems that the observed morphological differences are ascribed to the different growth mechanisms brought about by the various solvents.

The morphology of the active materials in a hydrothermal process is determined by many growth parameters such as reaction rate, viscosity (and concentration) of the solvent and active sites available on the substrate surface. The organic solvents used in this study had different viscosities and polarities, which played a key role in determining the observed morphologies by changing the reaction speed. These organic solvents formed micelles on the substrate surface, which served as a template during the hydrothermal growth. However, in the aqueous case (DI water), these micelles were able to form even at low viscosity due to electrostatic forces of attraction. Furthermore, the viscosity of water (0.7972 mpa s) is lower than that of ethanol (0.983 mpa s), ethylene glycol (16.1 mpa s), and glycerol (1412 mpa s). As viscosity increases, it subsequently reduces the growth rate of active materials, which could be the reason for the arrested growth of $CuCo_2O_4$ in the presence of glycerol (Figure 1d). Thus, a particular morphological modification might have enhanced the electrochemically active surface area (ECSA) of the film, which was beneficial for its electrochemical properties.

The formation of mesoporous nanosheet, cubic, compact granular, and agglomerated spherical-like structures were clearly revealed in the TEM analyses. Figure 3a shows the TEM, HR-TEM and SAED images of the CCO_{nS} sample whereas the data for the CCO_C, CCO_G, and CCO_S samples are presented in the Figure S2 (Supplementary Information). Figure 3a shows the TEM image of a single nanosheet from the CCO_{nS} sample. The randomly distributed white regions throughout the nanosheet revealed the formation of nanopores on its surface were also clearly identified by the randomly distributed black regions on the surface of the nanosheet in the SEM image (Figure 3a, inset). The clear lattice fringe regions observed in the HR-TEM image (Figure 3b) suggest the formation of polycrystalline $CuCo_2O_4$, which was also detected for the CCO_C, CCO_G, and CCO_S samples. The observed lattice distances (Figure 3c) were associated with the d-spacing of the cubic $CuCo_2O_4$ phase. The SAED pattern (Figure 3d) shows many diffraction spots, thereby confirming the polycrystalline nature of the CCO_{nS} sample.

We carried out CV, GCD and EIS measurements to systematically explore the electrochemical properties of the CCO electrodes for potential use in supercapacitive applications. Figure 4a shows the CV curves for the CCO electrodes at a scan rate of 5 mV s^{-1} (the scan rate dependent CV curves are presented in Figure S3 in the Supplementary Information). The measured CV curves revealed the typical pseudocapacitive nature of the CCO electrodes. Two distinct redox peaks in the anodic and cathodic sweeps were associated with the reversible Faradaic reactions of $Co^{3+} \leftrightarrow Co^{4+}$ and $Cu^{2+} \leftrightarrow Cu^{+}$ transitions at the electrode-electrolyte interface in the alkaline KOH electrolyte due to the insertion and de-insertion of $(OH)^-$ ions, respectively. The electrochemical redox reactions at the interface were

$$CuCo_2O_4 + H_2O \leftrightarrow CoOOH + Cu(OH)_2 \quad (1)$$

$$CoOOH + (OH)^- \leftrightarrow CoO_2 + H_2O + e^-. \quad (2)$$

As the scan rate increased the oxidation-reduction peak currents also increased linearly and the peak position shifted towards a higher voltage, indicating that the electronic and ionic transport becomes effective even at the high scan rates,[46,47] behaviour which is associated with polarization during the redox reaction. Among the CCO electrodes, the CCO_{nS} electrode attained the highest CV peak current density, implying its superior electrochemical activity.

Figure 4b shows the anodic peak current density (J_{ap}) as a function of the square root of the scan rate ($v^{1/2}$). The observed linear relationship between J_{ap} and $v^{1/2}$ suggests the pseudocapacitive nature of the CCO electrodes only limited by the diffusion of $(OH)^-$ ions to the electrochemically active sites.[47-49] The following equation describes the correlation between the peak current and the diffusion coefficient:

$$J_{ap} = (2.69 \times 10^5)\, C_o^* A\, n^{3/2}\, D_o^{1/2}\, v^{1/2}, \quad (3)$$

where C_o^* represents the concentration of the reactants, A indicates the area of the CCO electrode, n is the number of electrons transferred, and D_o represents the diffusion coefficient.[24,41] To compare the diffusion of $(OH)^-$ ions to the active sites of the CCO_{nS}, CCO_C, CCO_G, and CCO_S electrodes during the electrochemical process, the relative diffusion

coefficient D_r is defined with respect to the CCO_{nS} electrode using Eq. (4) (it is assumed that the $CuCo_2O_4$ electrodes have the same A, C_o^*, and n values):

$$D_r \equiv D_{CCOnS} / D_{SV} = [(J_{ap} / v^{1/2})_{CCOnS} / (J_{ap} / v^{1/2})_{SV}]^2, \quad (4)$$

where the subscript *SV* represents the variation of solvents during hydrothermal growth. The D_r value was calculated as 1.51, 13.72, and 86.89 for the CCO_C, CCO_G, and CCO_S electrodes, respectively. The obtained D_r values revealed that the CCO_{nS} electrode had the largest diffusion coefficient, which is presumably because of the lowest charge transfer resistance for ion diffusion (Figure 6b).

The accessible ECSA for an electrochemical reaction can be estimated by analysing the electrochemical double-layer capacitance of the catalytic surface. The linear charging region of the CV curves from 95 to 205 mV (Figure 4c) was linked to the electrochemical capacitance in the non-Faradaic region (Figure 4d) shows the $J_{DL}(v)$ curves of the CCO electrodes measured at 0.15 mV). The scan rate v-dependent capacitive current $J_{DL}(v)$ was determined by the charge accumulation in the linear charging region, which is given by

$$J_{DL} = C_{DL} \cdot v, \quad (5)$$

where C_{DL} stands for the specific capacitance of the non-Faradaic region, and solely consists of the slope of the $J_{DL}(\nu)$ curve. The ECSA of the CCO electrodes was then calculated as

$$\text{ECSA} = C_{DL} / Ce, \quad (6)$$

where Ce (0.04 mF cm^{-2} for the KOH electrolyte) represents the specific capacitance of the alkaline solution.[50] The CCO_{nS} electrode showed a considerably larger ECSA value of 7595 cm^{-2} compared to those of the other three samples: 5380 cm^{-2} for CCO_C, 743 cm^{-2} for CCO_G, and 538 cm^{-2} for CCO_S. This ECSA analysis was in good agreement with the considerably enhanced ion diffusion of the CCO_{nS} electrode.

Figure 5a shows the galvanostatic charge-discharge (GCD) curves for the CCO electrodes at 1 A g^{-1}. It is clearly evident that the CCO_{nS} electrode had the longest discharge time compared to the other three CCO electrodes. The specific capacitance of the CCO electrodes from the

GCD curves was calculated as

$$C_s = (I \times \Delta t) / (m \times \Delta V), \quad (7)$$

where I is the response current (mA), Δt is the discharge time (s), m is the loading mass of the electrode (g), and ΔV (V) is the applied potential window. The calculated specific capacitances for the $CCO_{nS,}$ CCO_C, CCO_G, and CCO_S electrodes at 1 A g^{-1} were 1658, 1392, 414, and 344 F g^{-1}, respectively. As the current density increased the discharge time decreased due to incomplete Faradaic reactions (Figure S4, Supplementary Information). The discharge time decreased with increasing current density, and shortened more quickly in the high current density region due to the non-linear behaviour of the ion diffusion at the electrode-electrolyte interface.[51] Figure 5b shows the calculated specific capacitances of the CCO electrodes as a function of current density. The maximum specific capacitance was obtained from the mesoporous CCO_{nS} electrode at 1 A g^{-1}, which decreased with increasing current density. Thus, it attained excellent capacitance retention of ~ 59% at a high current density of 20 A g^{-1}, confirming that it was optimized for supercapacitive electrochemical activity.

The restoration capability of the CCO electrodes at high and low current rates could lead to these pseudocapacitive electrodes being used in various practical applications. Figure 5c shows the specific capacitance restoration capability of the CCO electrodes at various current densities. When the current density rate was increased from 1 to 20 A g^{-1}, the specific capacitance of the $CCO_{nS,}$ CCO_C, CCO_G, and CCO_S electrodes retained 59, 54, 59, and 62%, respectively. As the current density deceased to 2 A g^{-1}, the restoration capability of the CCO electrodes was ~ 87, 87, 82, and 78%, respectively.

Long-term cyclic stability is a key parameter of SCs to be used practically with good endurance. We tested 5,000 charge/discharge cycles for the CCO electrodes at 20 A g^{-1} shown in Figure 5d. After 400 continuous charge/discharge cycles, the specific capacitance of CCO_{nS} increased from 974 to 1001 F g^{-1} and this increasing propensity of capacitance over cycling can be attributed to the electrode activation process enhancing the participating ECSA.[1] All of the

CCO electrodes showed good long-term cyclic stability up to 5,000 cycles; the $CCO_{nS,}$ CCO_C, CCO_G, and CCO_S electrodes attained the capacitance retention of ~ 90, 75, 53, and 41% after 5,000 charge/discharge cycles, respectively, with this decrement in capacitance value probably being because of slightly improved resistance. Figure S5b shows Nyquist plots of the CCO_{nS} electrode before and after ($CCO_{nS\text{-}25\ h}$) cyclic stability testing. The charge transfer resistance of CCO_{nS} electrode was slightly increased from 131 to 148 mΩ, resulting in lower capacity retention. The better capacity retention of CCO_{nS} than the other CCO electrodes was presumably due to the structural integrity of CCO nanosheet electrode, which was the benefit of directly growing the active material on the 3D substrate.

EIS measurements were used to explore the fundamental electron transfer kinetics of the CCO electrodes. The Nyquist plots of $CCO_{nS,}$ CCO_C, CCO_G, and CCO_S electrodes shown in Figure 6a consist of a partial semicircle and a straight line in the high and low-frequency regions, respectively. The semicircle feature can be attributed to the charge transfer resistance (R_{ct}) of the material and the straight-line (Warburg impedance; W) represents the redox behaviour of the CCO electrodes.[52,53] The intersection of the semicircles at the X-axis indicates the internal resistance of the electrodes (R_s), which is a combination of the intrinsic resistance of the substrate and electrolyte resistance in the electrochemical system. Impressively, the CCO_{nS} electrode exhibited lower R_s (0.61 Ω) and R_{ct} (131 mΩ) values than those of CCO_C (0.618 Ω and 201 mΩ), CCO_G (0.653 mΩ and 249 mΩ), and CCO_S (0.672 mΩ and 273 mΩ). This indicates that the rapid electron transfer at the CCO_{nS} electrode surface was as a result of the synergistic effect arising from copper and cobalt in the bimetallic oxides, the 2D nanosheet morphology, and the mesoporous structure. The excellent performance of the CCO_{nS} can be ascribed to the synergistic effect of the Cu-Co bimetal in the CCO, which might have varied the surface states of the electron energy that enhanced the pseudocapacitive performance of the CCO electrodes. CCO_{nS} is composed of thin nanosheets with porous structure that most likely assisted the electrolyte in transporting and interacting with the active

sites due to the highly conductive electron transport medium significantly improving the electrochemical stability of the electrode.

Figure 6b reveals the influence of solvent viscosity on the measured specific capacitance (C_s) and charge transfer resistance (R_{ct}) of the electrodes. Because C_s is proportional to the specific area and R_{ct} is inversely proportional to it, we expected that measured C_s and the extracted R_{ct} would show opposing behaviour. Indeed, the solvent viscosity increased the C_s and R_{ct} exhibited the anticipated opposing behaviour, as evidenced by the data in Figure 6b. Nanosheet-like morphology was obtained using low viscosity solvents because the latter might have caused fast reaction rates. High viscosity solvents reduced the reaction rate, which eventually restricted the nucleation and growth of the CCO material. Thus, the variation in morphology with viscosity resulted in different specific areas for active redox reactions, which in turn led to variation in the electrochemical performance.

Ragone plots for power (P) and energy (E) densities are calculated from the charge/discharge measurements using the following equations:

$$E = 0.5 \times C_s \times \Delta V^2, \quad (8)$$

$$P = E / \Delta t . \quad (9)$$

As the current density increased, the diffusion time became shorter and the specific capacitance decreased as shown in Figure 5c. The optimized CCO_{nS} electrode attained a very high energy density of 132.64 Wh kg^{-1} at a given power density of ~ 0.72 kW kg^{-1} with a steep slope in the *P-E* relationship which indicated its superior supercapacitive performance even at high current rates.

Electrochemical water splitting

The OER activity of the CCO electrodes was investigated using linear sweep voltammetry (LSV) at a scan rate of 5 mV s^{-1} in 1 M KOH the results of which are shown in Figure 7a. The CCO electrodes exhibited low onset overpotentials of 294 to 399 mV to drive a current density of 20 mA cm^{-2}, and the CCO_{nS} catalyst attain the lowest overpotential of 294 mV. This superior

catalytic activity is attributed to the mesoporous architecture of its nano-sheets, its high catalytic surface area, and its low electronic resistance during electrochemical reactions.

Figure 7b protrays a Tafel plot of the CCO electrodes. The linear portion of the Tafel curve was fitted using the Tafel equation $\eta = a + b \log j$, where η represents the overpotential, a is the fitting parameter, b is the Tafel slope, and j is the current density. The lowest Tafel slope of 117 mV dec^{-1} was obtained by the CCO_{nS} catalyst, revealing its enhanced reaction kinetics for the OER.

The overpotential of the catalysts could be comparatively understood by plotting their current rate performance, as shown in Figure 7c. As the current density increased by a steps of 10 mA cm^{-2} the overpotential also increased linearly. The CCO_{nS} catalyst exhibited the lowest overpotential at each current density. Since long-term electrochemical OER stability is a key characteristic for the practical use of a catalyst, the OER stability of the CCO_{nS} electrode was tested at static current levels of 20 and 50 mA cm^{-2} (Figure 7d). It can be seen that the potential increased initially due to the activation process, thereby producing highly oxidized intermediates, and then remained stable over 25 hours. Continuous and vigorous gas evolution was observed on the surface of the catalyst during the stability measurements, the bubbles from which dissipated rapidly into the electrolyte. The almost identical LSV curves (with iR correction) of the optimized CCO_{nS} catalyst before and after the stability test (Figure S5a) revealed its excellent durability for the OER in an alkaline solution.

In summary, we fabricated $CuCo_2O_4$ bifunctional electrodes with different morphologies via a hydrothermal method. Various solvents with different viscosities were used to vary the growth kinetics. As the solvent viscosity increased, the surface morphology of the CCO films became nano-sheet, cubic, compact granular, and agglomerated embossing structures, without the underlying crystallinity and chemical composition being altered. The best bifunctional electrochemical properties were obtained from the CCO nanosheet film with a maximum specific capacitance of 1658 F g^{-1} at a current density of 1 A g^{-1} with restoration capability of

~ 99% at 2 A g^{-1}. Moreover, it was able to deliver capacity retention of ~ 90% at a high current density of 20 A g^{-1} even after 5,000 charge/discharge cycles, with a coulombic efficiency of ~ 93%, and a superior energy density of 132.64 Wh kg^{-1} was obtained at a power density of 0.72 kW kg^{-1}. Furthermore, it exhibited superior water splitting properties by attaining an overpotential of 294 mV at 20 mA cm^{-2} with the lowest Tafel slope of 117 mV dec^{-1} and excellent long-term stability at high current densities. The observed morphology dependent bifunctional properties of the CCO film were mainly attributed to different effective electrochemically active sites.

Experimental Section

Preparation of the thin film electrodes: All chemicals were of analytical grade purity purchased from Sigma Aldrich and used as received. $CuCo_2O_4$ electrode films were directly fabricated on Ni foam substrates via a one-step hydrothermal synthesis. In a typical synthesis, 3 mmol $CuCl_2 \cdot 2H_2O$ and 6 mmol $CoCl_2 \cdot 6H_2O$ were dissolved in 40 ml deionized (DI) water followed by the addition of 18 mmol urea (CH_4N_2O) under strong stirring for 30 min at room temperature. The mixture solution and pre-cleaned Ni foam substrate were transferred into a 100 ml Teflon-lined stainless steel autoclave and maintained at 120 °C for 6 h in a muffle furnace. After unaided cooling to room temperature, the samples were washed with DI water and ethanol, dried at room temperature followed by calcination at 300 °C for 2 h in a tubular furnace at a ramping rate of 1 °C min^{-1} in ambient air. All growth parameters remained unchanged except for the used solvent. Afterwards, the $CuCo_2O_4$ films fabricated using DI water, ethanol, ethylene glycol, and glycerol were denoted as CCO_{nS}, CCO_C, CCO_G, and CCO_S, respectively.

Material Characterization: The crystallinity of the $CuCo_2O_4$ films was characterized using X-ray diffractometry (XRD) with CuK_α radiation (Rigaku Smartlab, λ = 1.54056 Å) operated at 40 kV with an applied current of 30 mA and a scanning rate of 2° min^{-1}. The morphological and compositional properties of the $CuCo_2O_4$ electrode films were analysed using field emission scanning electron microscopy (FE-SEM) and energy dispersive spectroscopy (EDS;

Model: JSM-6701F, Japan) operated at 15 kV. EDS spectra were obtained at 5,000x magnification. X-ray photoelectron spectroscopy (XPS) measurement was carried out using a PHI 5000 VersaProbe (ULVAC PHI, Japan). The C 1s position of carbon contaminant in the vacuum chamber of the XPS instrument (284.8 eV) was used to calibrate the binding energies of the elements. Transmission electron microscope (TEM, JEOL-3000F), high resolution TEM (HR-TEM) images, and selected-area electron diffraction (SAED) patterns were obtained at 300 kV.

Electrochemical measurements: The electrochemical properties of the $CuCo_2O_4$ thin film electrodes were investigated using a conventional three-electrode electrochemical system (Princeton Applied research, VersaSTAT). Cyclic voltammetry (CV), galvanostatic charge/discharge (GCD), and electrochemical impedance spectroscopy (EIS) measurements were performed in 2 M aqueous KOH electrolyte while the OER activities were investigated using linear sweep voltammetry (LSV) in 1 M KOH. The $CuCo_2O_4$ films were used as the working electrodes, while platinum mesh and the saturated calomel electrode (SCE) served as the counter and reference electrodes, respectively. LSV testing was performed at 5 mV s^{-1} in a potential range between 0 and 0.6 V (vs. SCE) and the GCD test was conducted in a stable potential window from 0 to 0.4 V (vs. SCE) at different current densities. Electrochemical impedance spectroscopy (EIS) measurements were carried to help understand the charge-transfer kinetics at the electrode/electrolyte interface in the frequency range between 1 Hz and 10 kHz with an applied AC signal voltage of 10 mV.

Supporting Information

Supporting Information is available from the Wiley Online Library or from the author.

Acknowledgments

The authors would like to thank the financial support from the National Research Foundation (NRF) of Korea (Grant nos. 2015M2A2A6A02045251, 2015R1D1A1A01058851, 2015R1A2A2A01004782, and 2015R1A2A1A15054906).

References

[1] S. Vijayakumar, S. H. Lee, K. S. Ryu, *Electrochimica Acta*, **2015**, *82*, 979.

[2] P. Simon, Y. Gogotsi, *Nature Mater*. **2008**, *7*, 845.

[3] Q. Wang, D. Chen, D. Zhang, *RSC Adv*. **2015**, *5*, 96448.

[4] H. Zhao, C. Wang, R. Vellacheri, M. Zhou, Y. Xu, Q. Fu, M. Wu, F. Grote, Y. Lei, *Adv. Mater*. **2014**, *26*, 7654.

[5] J. Zhao, H. Lai, Z. Lyu, Y. Jiang, K. Xie, X. Wang, Q. Wu, L. Yang, Z. Jin, Y. Ma, J. Liu, Z. Hu, *Adv. Mater*. **2015**, *27*, 3541.

[6] E. Lim, H. Kim, C. Jo, J. Chun, K. Ku, S. Kim, H. I. Lee, I. S. Nam, S. Yoon, K. Kang, J. Lee, *ACS Nano*, **2014**, *8*, 8968.

[7] Q. Wang, J. Xu, X. Wang, B. Liu, X. Hou, G. Yu, P. Wang, D. Chen, G. Shen, *ChemElectroChem*, **2014**, *1*, 559.

[8] P. Poizot, S. Laruelle, S. Grugeon, L. Dupont, J. M. Tarascon, *Nature*, **2000**, *407*, 496.

[9] Q. F. Wang, B. Liu, X. F. Wang, S. H. Ran, L. M. Wang, D. Chen, G. Z. Shen, *J. Mater. Chem. A*, **2012**, *22*, 21647.

[10] P. C. Chen, G. Z. Shen, S. Sukcharoenchoke, C. W. Zhou, *Appl. Phys. Lett.* **2009**, *94*, 043113.

[11] G. Q. Zhang, H. B. Wu, H. E. Hoster, M. B. Chan-Park, X. W. Lou, *Energy Environ. Sci.* **2012**, *5*, 9453.

[12] Q. F. Wang, X. F. Wang, B. Liu, G. Yu, X. J. Hou, D. Chen, G. Z. Shen, *J. Mater. Chem. A*, **2013**, *1*, 2468.

[13] Z. Chen, Y. C. Qin, D. Weng, Q. F. Xiao, Y. T. Peng, X. L. Wang, H. X. Li, F. Wei, Y. F. Lu, *Adv. Funct. Mater*. **2009**, *19*, 3420.

[14] C. G. Liu, Z. N. Yu, D. Neff, Z. Aruna, B. Z. Jang, *Nano Lett*. **2010**, *10*, 4863.

[15] C. Z. Yuan, L. Yang, L. R. Hou, L. F. Shen, X. G. Zhang, X. W. Lou, *Energy Environ. Sci*. **2012**, *5*, 7883.

[16] P. C. Chen, G. Z. Shen, Y. Shi, H. T. Chen, C. W. Zhou, *ACS Nano*, **2010**, *4*, 4404.

[17] G. P. Wang, L. Zhang, J. J. Zhang, *Chem. Soc. Rev*. **2012**, *41*, 797.

[18] J. M. Tarascon, M. Armand, *Nature*, **2001**, *414*, 359.

[19] J. Chen, A. I. Minett, Y. Liu, C. Lynam, P. Sherrell, C. Wang, G. G. Wallace, *Adv. Mater*. **2008**, *20*, 566.

[20] Y. Zhang, M. Ma, J. Yang, C. Sun, H. Su, W. Huang, X. Dong, *Nanoscale*, **2014**, *6*, 9824.

[21] B. E. Conway, *J. Electrochem. Soc*. **1991**, *138*, 1539.

[22] R. B. Rakhi, D. Cha, W. Che, H. N. Alshareef, *Nano Lett*. **2012**, *12*, 2559.

[23] P. Simon and Y. Gogotsi, *Nat. Mater*. **2008**, *7*, 845.

[24] S. Cho, J. Han, J. Kim, Y. Jo, H. Woo, S. Lee, A. T. A. Ahmed, H. C. Chavan, S.M. Pawar, J. L. Gunjakar, J. Kwak, Y. Park, A. I. Inamdar, H. Kim, H. S. Kim, H. Im. *Current Applied Physics*, **2017**,*17*, 1189-1193.

[25] W. Chen, R. B. Rakhi, L. B. Hu, X. Xie, Y. Cui, H. N. Alshareef, *Nano Lett*. **2011**, *11*, 5165.

[26] R. F. Service, *Science*, **2006**, *313*, 902.

[27] C. Z. Yuan, B. Gao, L. F. Shen, S. D. Yang, L. Hao, X. J. Lu, F. Zhang, L. J. Zhang, X. G. Zhang, *Nanoscale*, **2011**, *3*, 529.

[28] C. Liu, F. Li, L. P. Ma, H. M. Cheng, *Adv. Mater*. **2010**, *22*, E28.

[29] J. Chmiola, G. Yushin, Y. Gogotsi, C. Portet, P. Simon, P. L. Taberna, *Science*, **2006**, *313*, 1760.

[30] J. R. Miller, P. Simon, *Science*, **2008**, *321*, 651.

[31] M. C. Liu, L. B. Kong, C. Lu, X. M. Li, Y. C. Luo, L. Kang, *RSC Adv*. **2012**, *2*, 1890.

[32] J. Cheng, H. Yan, Y. Lu, K. Qiu, X. Hou, J. Xu, L. Han, X. Liu, J. K. Kim, Y. Luo, *J. Mater. Chem. A*, **2015**, *3*, 9769.

[33] M. Armand, J. M. Tarascon, *Nature*, **2008**, *451*, 652.

[34] A. S. Arico, P. Bruce, B. Scrosati, J. M. Tarascon, W. V. Schalkwijk, *Nat. Mater*. **2005**, *4*, 366.

[35] Y. S. Luo, J. S. Luo, J. Jiang, W. W. Zhou, H. P. Yang, X. Y. Qi, H. Zhang, H. J. Fan, Y. W. Y. Denis, C. M. Li, T. Yu, *Energy Environ*. *Sci*. **2012**, *5*, 6559.

[36] J. Shen, J. Tang, P. Dong, Z. Zhang, J. Jia, R. Baines, M. Ye, *RSC Adv*. **2016**, *6*, 13456.

[37] W. Fu, C. Zhao, W. Han, Y. Liu, H. Zhao, Y. Ma, E. Xie, *J. Mater. Chem. A*, **2015**, *3*, 10492.

[38] M. Kuang, X. Y. Liu, F. Dong, Y. X. Zhang, *J. Mater. Chem. A*, **2015**, *3*, 21528.

[39] W. Kong, C. Lu, W. Zhang, J. Pub, Z. Wang, *J. Mater. Chem. A*, **2015**, 3, 12452.

[40] A. Pendashteh, M. S. Rahmanifar, R. B. Kaner, M. F. Mousavi, *Chem. Commun*. **2014**, *50*, 1972.

[41] A. T. A. Ahmed, H. S. Chavan, Y. Jo, S. Cho, J. Kim, S. M. Pawar, J. L. Gunjakar, A. I. Inamdar, H. S. Kim, H. Im, *Journal of Alloys and Compounds*, **2017**, *724*, 744.

[42] X. Wang, X. Han, M. Lim, N. Singh, C. L. Gan, M. Jan and P. S. Lee, *J. Phys. Chem. C*, **2012**, *116*, 12448.

[43] J. Tang, Y. Ge, J. Shen, M. Ye, *Chem. Commun*. **2016**, *52*, 1509.

[44] Q. Hu, W. Ma, G. Liang, H. Nan, X. Zheng, X. Zhang, *RSC Adv*. **2015**, 5, 84974.

[45] G. Zhang, X. W. Lou, *Adv. Mater*. **2013**, *25*, 976.

[46] T. Peng, T. Zhao, Q. Zhou, H. Zhou, J. Wang, J. Liu, Q. Liu. CrystEngComm **2015**, 17, 7583-7591.

[47] S. Liu, K. S. Hui, K. N. Hui, *ACS Appl. Mater. Interfaces*, **2016**, 8, 3258.

[48] M. Sun, J. Tie, G. Cheng, T. Lin, S. Peng, F. Deng, F. Ye, Lin, Yu, *J. Mater Chem. A*,

2015, *3*, 1730.

[49] X. Li, Q. Li, Y. Wu, M. Rui, H. Zeng, *ACS Appl. Mater. Interfaces*, **2015**, 7, 19316-19323.

[50] R. Patel, A. I. Inamdar, B. Hou , S. Cha, A. T. Ansari, J. L. Gunjakar, H. Im, H. S. Kim, *Current Applied Physics*, **2017**, *17*, 501.

[51] Z. S. Hong, Y. Cao, J. F. Deng, *Materials Letters*, **2002**, *52*, 34.

[52] M. Guo, J. Balamurugan, T. D. Thanh, N. H. Kim, J. H. Lee, *J. Mater. Chem. A*, **2016**, *4*, 17560.

[53] L. Qian, L. Gu, L. Yang, H. Yuan, D. Xiao, *Nanoscale*, **2013**, *5*, 7388.

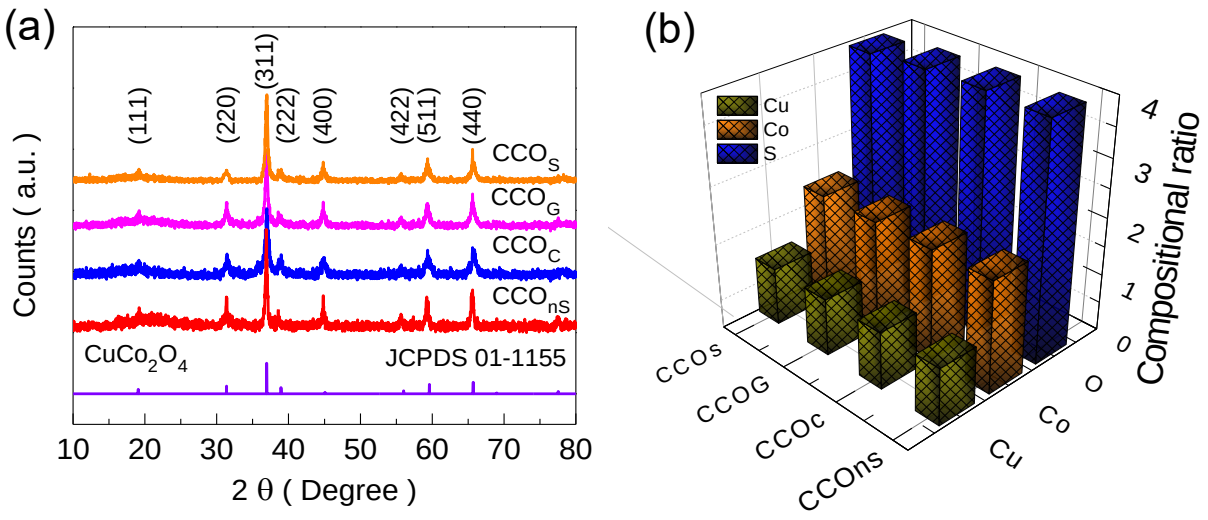

Figure 1. (a) XRD spectra and (b) an EDS histogram of the CCO films with nanosheet (nS), cubic (C), compact granular (G), and agglomerated embossing (S) morphologies. The distinctly similar XRD spectra and compositional ratios of the CCO films revealed that the used solvent

did not affect the underlying crystallinity and chemical composition of the film.

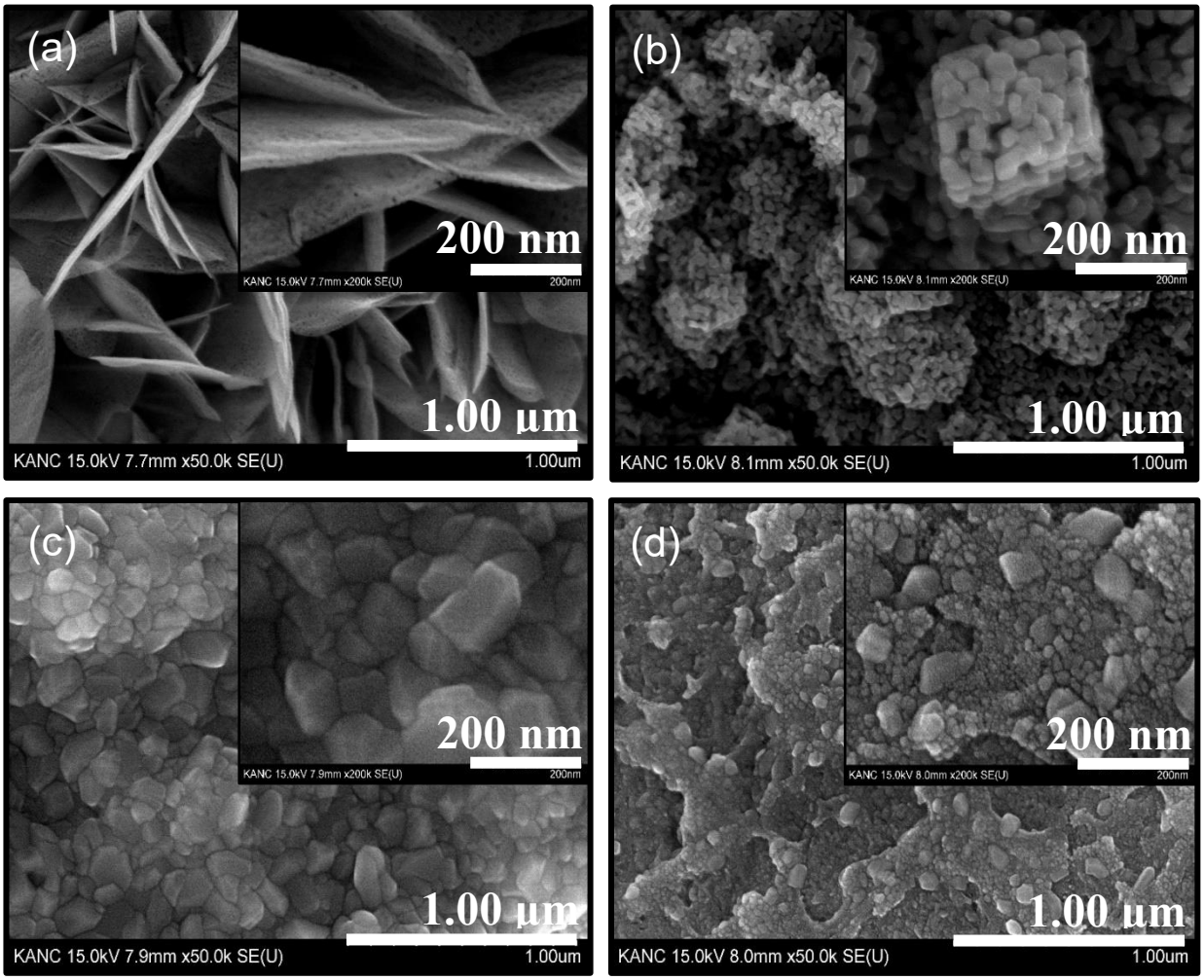

Figure 2. (a) FE-SEM images of the CCO films with different morphologies: (a) CCO_{nS} with a mesoporous nanosheet morphology, (b) CCO_{C} with a cubic morphology, (c) CCO_{G} with a compact granular morphology, and (d) CCO_{S} with an agglomerated embossing morphology. The inset in each image shows an enlarged view.

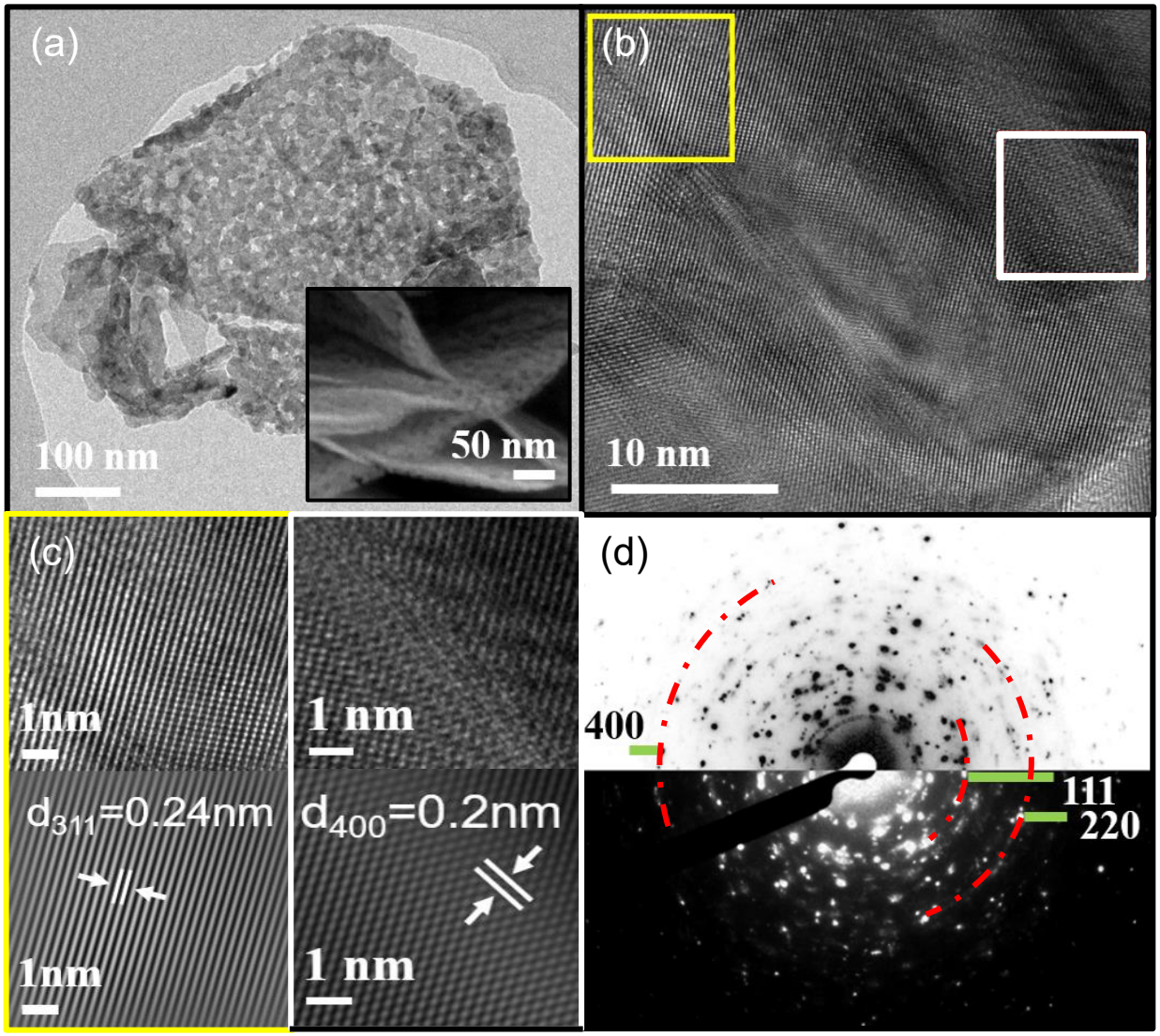

Figure 3. (a) TEM image of the CCO_{nS} sample. The inset shows a FE-SEM image of the nanosheets. Nanopores on the surface of the nanosheets are clearly visible and these correspond

to the white spots in the TEM image. (b) HR-TEM image revealing the polycrystalline nature of the CCO_{nS} nanosheets. (c) Enlarged view of the HR-TEM image (the boxes in Figure 3b) showing clear lattice fringes corresponding to d_{311} and d_{400} of $CuCo_2O_4$. (d) SAED pattern revealing the polycrystalline nature of the CCO_{nS} nanosheets.

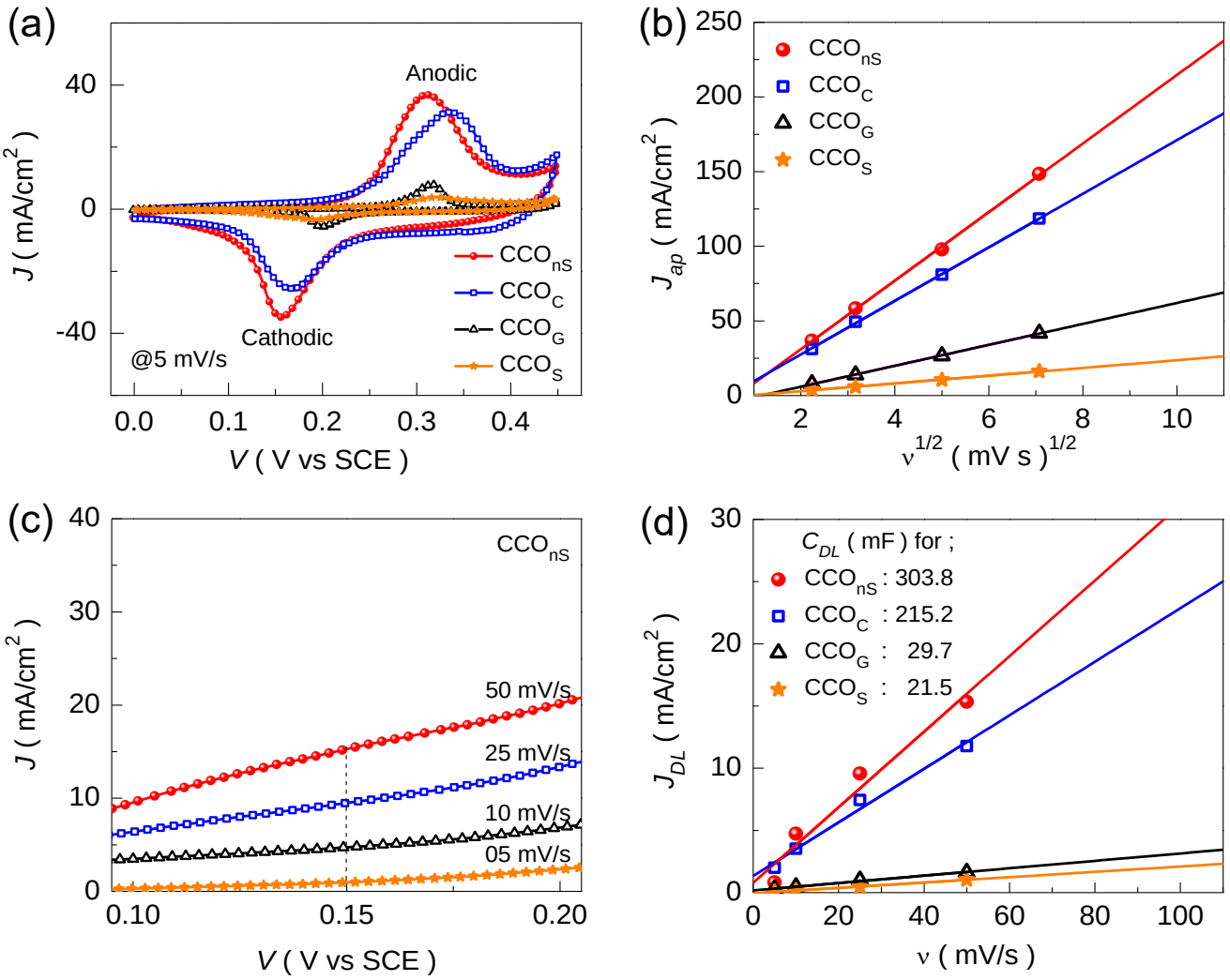

Figure 4. (a) CV curves at a scan rate of 5 mV s^{-1}. (b) Anodic-peak current density J_{ap} as a function of $v^{1/2}$. The linear relationship between J_{ap} and $v^{1/2}$ indicates pseudocapacitive nature

of the active electrode material. (c) CV curves of the CCO_{nS} electrode in the non-Faradaic linear charging region at different scan rates from 5 to 50 mV s^{-1}. (d) Non-Faradaic current density obtained from the CV curves in (c) at 0.15 V as a function of scan rate *v*. The lines are fitting curves obtained using Equation (5). The slope corresponds to the specific capacitance in the non-Faradaic region (C_{DL}).

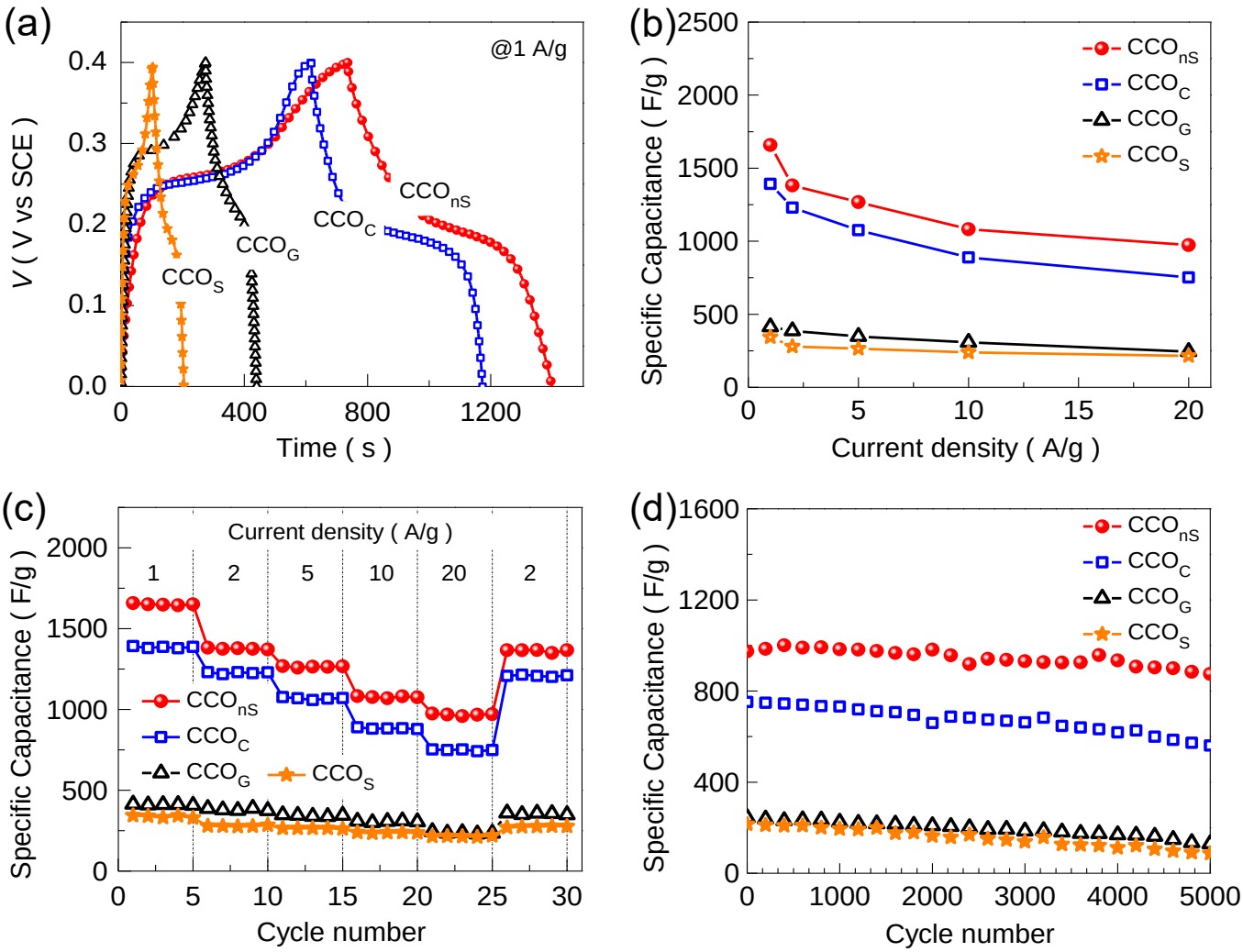

Figure 5. (a) GCD curves of the CCO electrodes at a current density of 1 A g^{-1}. (b) Specific capacitance of the CCO electrode as a function of current densities. (c) Rate capability of the

CCO electrodes from 1 to 20 A g^{-1}. (d) Specific capacitance of the CCO electrodes as a function of cycling up to 5,000 charge/discharge cycles.

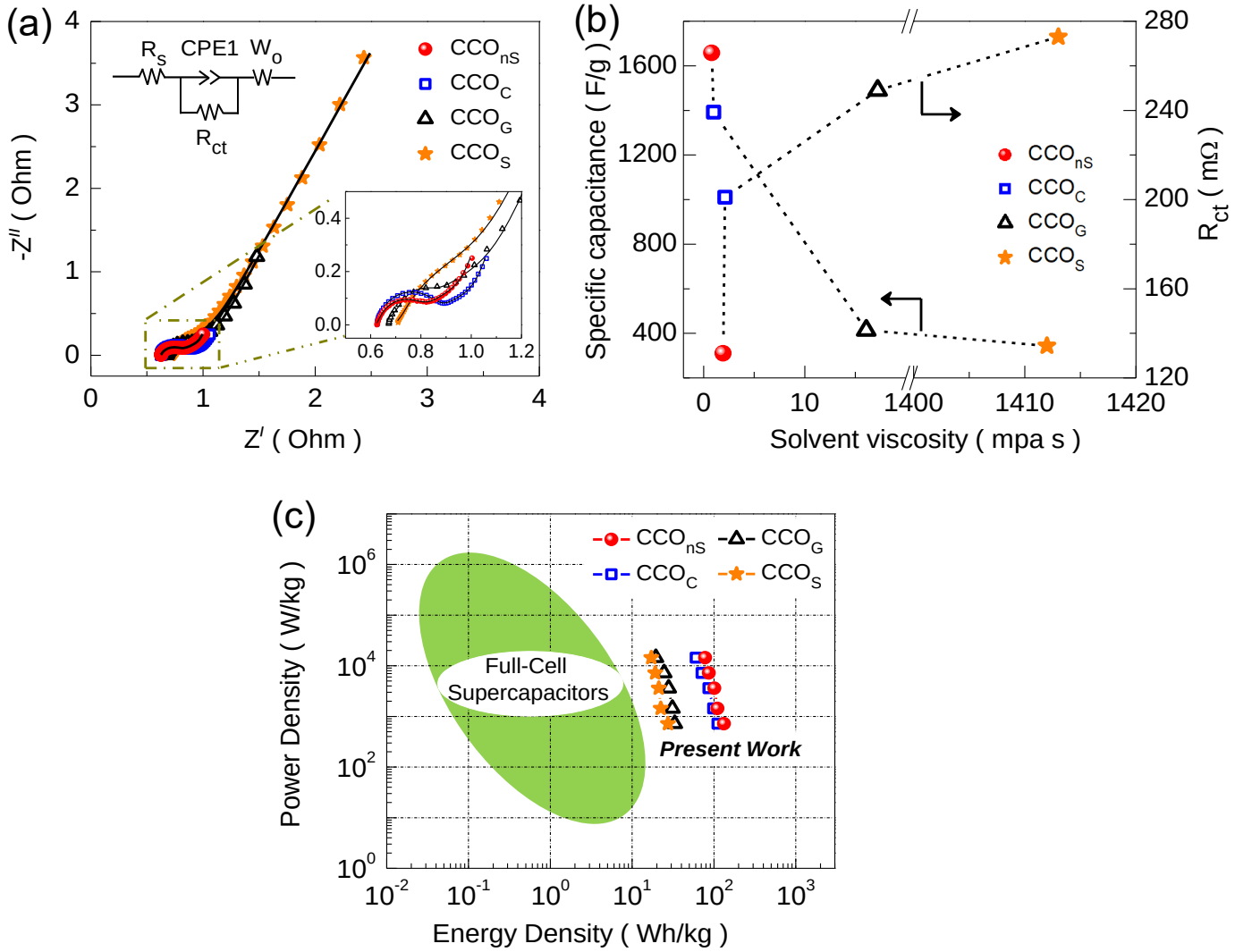

Figure 6. (a) Nyquist plots, (b) specific capacitance and R_{ct} as a function of solvent viscosity, and (c) Ragone plot of the CCO electrodes.

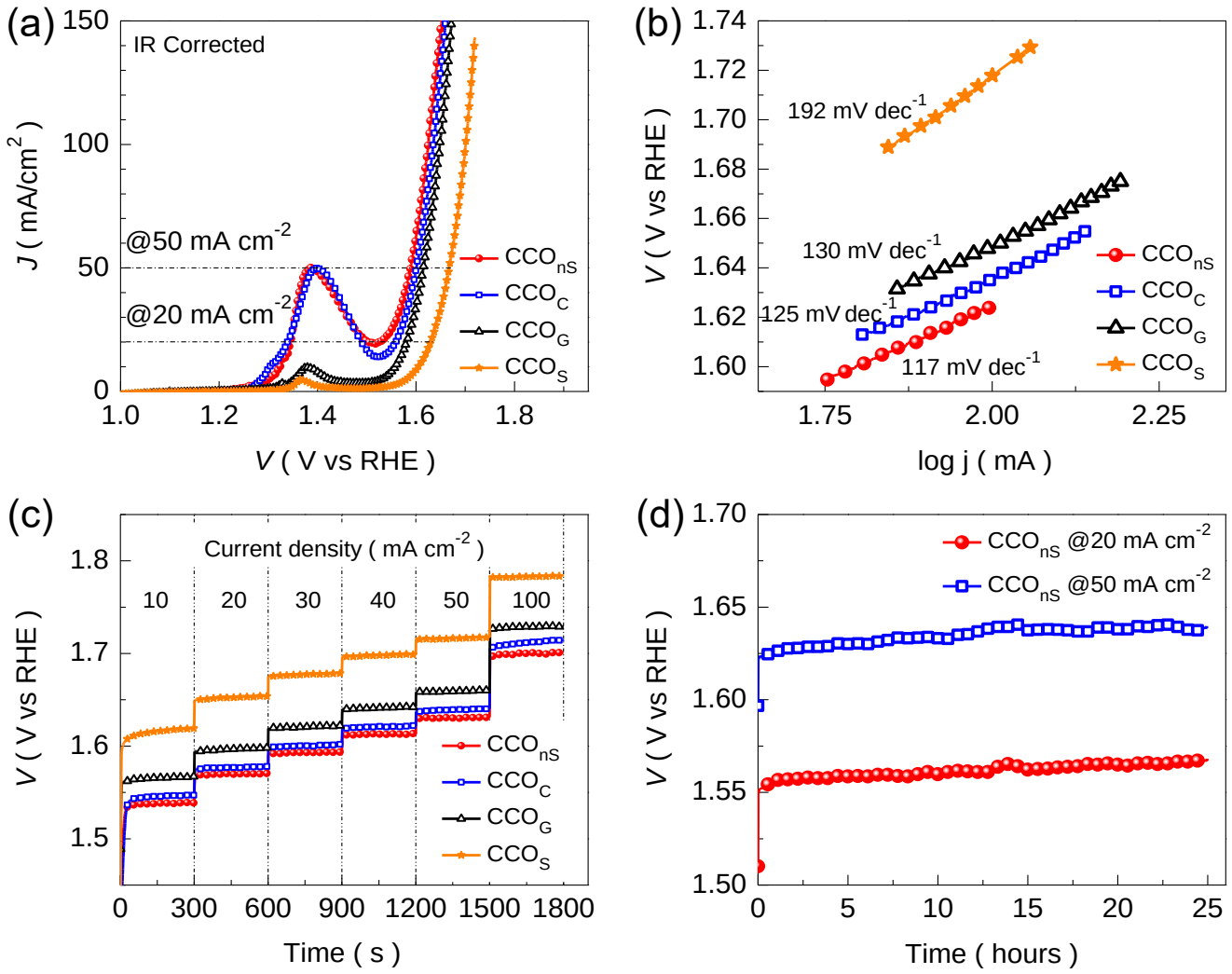

Figure 7. (a) LSV and (b) Tafel plots and (c) potential measured at various current densities ranging from 10 to 100 mA cm^{-2}, of the CCO electrodes. (d) Stability of the CCO$_{nS}$ electrode at 20 and 50 mA cm^{-2}.